Lab on a Chip

PAPER

View Article Online
View Journal | View Issue

Cite this: *Lab Chip*, 2025, **25**, 2234

Unveiling microbial single-cell growth dynamics under rapid periodic oxygen oscillations†

Keitaro Kasahara, [ab] Johannes Seiffarth, [ab] Birgit Stute, [a] Eric von Lieres, [ab] Thomas Drepper, [c] Katharina Nöh [a] and Dietrich Kohlheyer *[a]

Microbial metabolism and growth are tightly linked to oxygen (O_2). Microbes experience fluctuating O_2 levels in natural environments; however, our understanding of how cells respond to fluctuating O_2 over various time scales remains limited due to challenges in observing microbial growth at single-cell resolution under controlled O_2 conditions and in linking individual cell growth with the specific O_2 microenvironment. We performed time-resolved microbial growth analyses at single-cell resolution under a temporally controlled O_2 supply. A multilayer microfluidic device was developed, featuring a gas supply above a cultivation layer, separated by a thin membrane enabling efficient gas transfer. This platform allows microbial cultivation under constant, dynamic, and oscillating O_2 conditions. Automated time-lapse microscopy and deep-learning-based image analysis provide access to spatiotemporally resolved growth data at the single-cell level. O_2 switching within tens of seconds, coupled with precise microenvironment monitoring, allows us to accurately correlate cellular growth with local O_2 concentrations. Growing *Escherichia coli* microcolonies subjected to varying O_2 oscillation periods show distinct growth dynamics characterized by response and recovery phases. The comprehensive growth data and insights gained from our unique platform are a crucial step forward to systematically study cell response and adaptation to fluctuating O_2 environments at single-cell resolution.

Received 20th January 2025,
Accepted 6th March 2025

DOI: 10.1039/d5lc00065c

rsc.li/loc

Introduction

Microbes in natural habitats are exposed to external environmental changes and have evolved strategies to adapt to the surrounding conditions.[1] They proliferate in fluctuating environments on different time scales with different parameters, such as the availability of molecular oxygen (O_2),[2] nutrients,[3] pH,[4] temperature,[5] and light.[6] These fluctuating environmental conditions are pervasive, including the ocean[3] and soil,[5] as well as in animal hosts, such as in the nasal passage,[4] lung,[7] and intestine.[8] The timescale of fluctuation ranges from seasons (drying and wetting cycles in tropical forests),[9] days (day/night cycles),[5,6] and even minutes to seconds. In aquatic environments, for instance, microbes encounter new microenvironments in the time scale of seconds to minutes due to changes in surrounding conditions, displacement caused by fluid flow, and microbes' motility in the case of chemotactic bacteria.[10] The phycosphere, the nutrient and O_2 hotspot created by a phytoplankton cell, can dissipate in minutes or even faster due to diffusion and turbulence in fluid.[11,12] Fluctuating environments are also prevalent in biotechnological cultivation setups. Industrial large-scale bioreactors, for instance, stir large volumes of culture broth, often resulting in inefficient mixing and heterogeneous distribution of O_2 and nutrients, which could potentially lead to yield losses.[13–15] Investigating microbial behavior in fluctuating environments will, therefore, improve our understanding of microbial adaptation to external environmental changes and may offer insights into enhancing efficiency in industrial biotechnology.

Among the various environmental conditions, the availability of O_2 is one of the most critical for microbial growth and physiology. O_2 is intricately linked with a multitude of microbial processes, including iron homeostasis,[16] oxidative stress,[17] the development of pathogenic infections[18] and biofilm growth.[19] In addition to these microbial processes associated with O_2 availability, O_2 is also valuable as a primary electron acceptor for aerobic respiration in many microorganisms. In particular, facultative anaerobes, which are capable of growing under both aerobic and anaerobic conditions, adapt to changing O_2 environments by switching their metabolic pathways between

[a] *IBG-1: Biotechnology, Institute of Bio- and Geosciences, Forschungszentrum Jülich GmbH, 52425 Jülich, Germany. E-mail: d.kohlheyer@fz-juelich.de*
[b] *Computational Systems Biotechnology (AVT.CSB), RWTH Aachen University, Aachen, Germany*
[c] *Institute of Molecular Enzyme Technology, Heinrich Heine University Düsseldorf, Forschungszentrum Jülich GmbH, Jülich, Germany*

† Electronic supplementary information (ESI) available. See DOI: https://doi.org/10.1039/d5lc00065c

aerobic respiration and anaerobic respiration/fermentation.[20,21] This ability of facultative anaerobes to adapt to different O_2 environments has been extensively studied under single-shift O_2 environments. Previous studies have primarily focused on examining intracellular adaptation, such as transcriptome,[20] protein synthesis,[22] metabolome,[23] flux balance,[24] and phenotypic adaptation like growth fitness.[25] These studies have primarily been conducted in conventional cultivation setups, including microtiter plates, shaking flasks, and bioreactors. However, there is a lack of understanding regarding the cellular capability to adapt to rapidly fluctuating O_2 environments. Recent studies indicate that microbial behavior in fluctuating environments, where conditions shift within seconds to minutes, can differ significantly from behaviors observed in single-shift experiments.[26,27] Investigating the impact of O_2 fluctuations on microbial growth would facilitate a more comprehensive understanding of adaptation processes that remain to be elucidated.

The study of microbial responses to O_2 fluctuations has been hindered by several constraints. Conventional cultivation techniques do not facilitate rapid and precise changes in O_2 concentrations on the timescale of seconds to minutes, nor do they allow for simultaneous, high-resolution data acquisition. Environmental control in conventional laboratory cultivation setups is typically slow, with limited precision in maintaining homogeneity, temporal consistency, and resulting O_2 microenvironments. Additionally, these setups are often incompatible with fully resolving growth physiology under fluctuating O_2 conditions, as repetitive sampling is impractical without disrupting the culture. Consequently, it has been challenging to analyze the cellular response in terms of microbial growth and physiology caused by rapid O_2 fluctuations.

Today, microfluidic devices with precise environmental control and imaging at single-cell resolution are gaining attention as novel tools for creating oscillating environments on-chip and extracting microbial growth data with high temporal resolution. Previously reported microfluidic devices integrated O_2 control based on gas diffusion through air-permeable polydimethylsiloxane (PDMS) membrane.[28–32] Although some microfluidic systems have been developed to mimic oscillating conditions for pH, nutrients, and O_2,[27,33,34] detailed analysis linking microbial growth dynamics to fluctuating O_2 environments remains limited. To better understand microbial adaptation processes under rapid O_2 fluctuations, a platform is needed that allows for high-resolution, single-cell analysis of microbial growth, explicitly correlated with well-defined O_2 fluctuations (Fig. 1A).

In this work, we investigated, for the first time, the growth dynamics of the facultative anaerobe *Escherichia coli* (*E. coli*) MG1655 under O_2 oscillations occurring within minutes. To address the aforementioned limitations, we developed a double-layer microfluidic chip to facilitate rapid gas exchange within the cultivation chambers and frequent data acquisition accompanied by time-lapse microscopy to analyze cell division at the single-cell resolution (Fig. 1B). The PDMS microfluidic chip comprises two layers: an upper layer for gassing and a lower layer with multiple chambers for microbial cultivation. A thin intermediate PDMS membrane (65 μm) separates the two layers, facilitating rapid gas diffusion from the upper to the lower layer. The performance of the microfluidic chip was evaluated by spatially resolved O_2 imaging in the fluid channel using fluorescence lifetime imaging (FLIM) microscopy and a fluorescent O_2-sensitive dye. The microfluidic chip, automated time-lapse microscopy, and following deep-learning-based image analysis compose a versatile platform to analyze microbial growth and its correlation to applied O_2 oscillations. The platform was employed to cultivate *E. coli* under well-defined O_2 oscillating environments with varying oscillation periods, to examine cellular adaptation in a time-resolved manner. Here, we report periodically oscillating microbial growth dynamics composed of several adaptation phases and synchronized with applied O_2 oscillations.

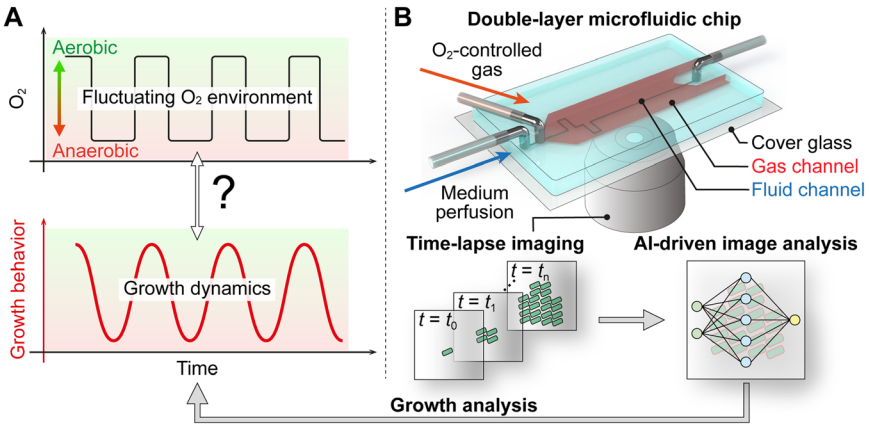

Fig. 1 Conceptual illustration of on-chip microbial growth analysis under rapidly oscillating O_2 environments. (A) Conceptual sketch of the proposed analysis of microbial growth dynamics in direct correspondence with external oscillating O_2 conditions. (B) Analytical platform comprising a double-layer microfluidic chip, time-lapse microscopy, and deep-learning-based image analysis, facilitating high spatiotemporal resolution in characterizing microbial growth under oscillating O_2 environments.

Results

On-chip O_2 control with the double-layer chip

The double-layer chip was fabricated by molding the upper and the lower layers separately and subsequently assembling them as shown in Fig. 2A. The fabricated chip is depicted in Fig. 2B. For visualization purposes, the top gas-layer channels (red) and bottom fluid-layer channels (blue) were filled with colored dyes. The SEM image (Fig. 2B (i)) depicts a series of cultivation chambers (50 μm × 30 μm × 1 μm) in which cells are trapped, and their growth can be observed over time *via* time-lapse imaging during cultivation. Each growth chamber is connected to two parallel medium supply channels (w = 100 μm, h = 10 μm), enabling continuous medium perfusion but mass transfer inside the chamber solely by diffusion. The cross-sectional photograph of the device (Fig. 2B (ii and ii′)) shows the PDMS membrane, which has a thickness of approximately 65 μm (fluid layer in the figure), physically separating the upper gas channel from the lower fluid channel.

For gas control optimization, the on-chip gassing performance was simulated using computational fluid dynamics with experimentally determined gas-inflow concentration profiles resulting from interconnected mass flow controllers. Therefore, the O_2 concentration was measured inside the supply tubing outlet under different gas-supply flow rates (100, 300, 600 mL min^{-1}) when no chip was installed (Fig. 2C). This was necessary because likely dead volumes in the mass flow controller setup were affecting the resulting switching performance, mostly when O_2 flow was fully switched off, and residual O_2 remained inside the non-perfused tubing and connectors. The residual O_2 was depleted relatively slowly by diffusion and delayed on-chip switching performance. When switching to higher O_2 levels, this problem was not observed since all interconnections were continuously perfused, and no controller was switched off. As depicted in Fig. 2C, the simulated O_2 level in the fluid channel exhibits a corresponding change from 21% to 0% when the O_2 level in the inlet gas is changed from 21% O_2 to 0% O_2 at t = 0 min. The simulation results indicated that the gas-supply volume flow rate was the limiting factor in our design, mostly impacting the exchange time of O_2 in the fluid channel rather than diffusion across the PDMS membrane. Based on the simulation results, the maximum total flow rate of N_2 and O_2 at 600 mL

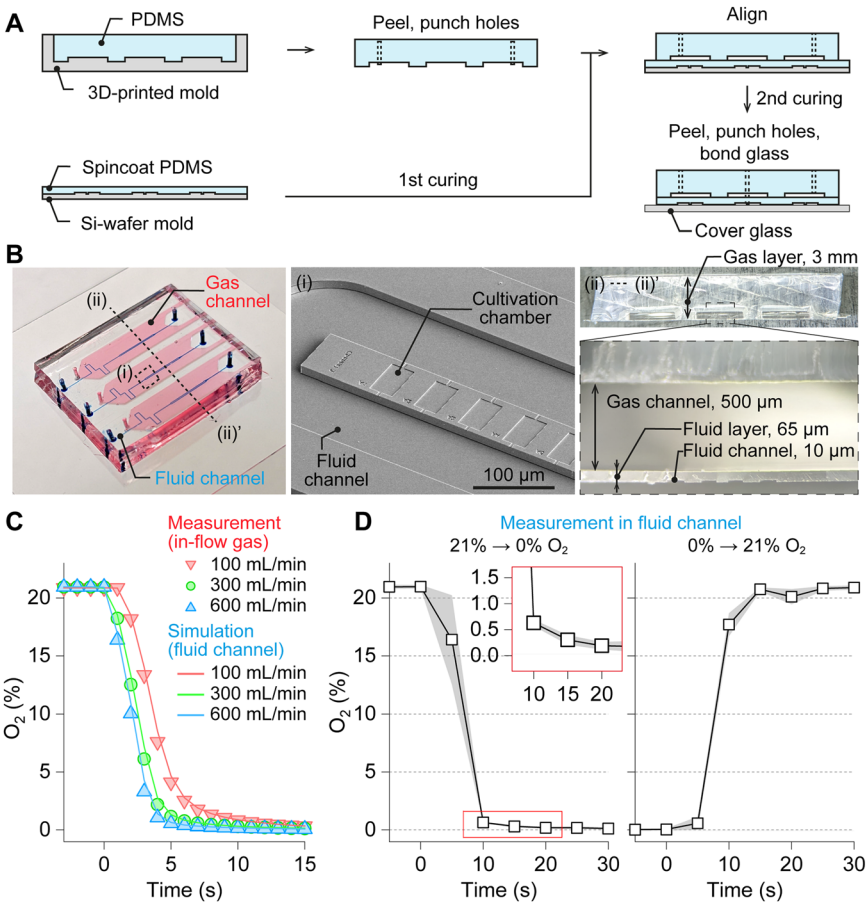

Fig. 2 Double-layer PDMS microfluidic chip enabling rapid gas control and single-cell imaging. (A) Schematic of the microfluidic chip fabrication process. (B) Fabricated microfluidic chip, with (i) an SEM image of the cultivation chambers and (ii and ii′) a cross-sectional view. (C) Measured O_2 level in the in-flow (plots) and simulated O_2 level at the center of the fluid channel (solid lines) following an O_2 shift from 21% to 0% at mass flow rates of 20, 100, and 600 mL min^{-1}. (D) Measured O_2 level in the fluid channel following an O_2 shift between 21% and 0%, with a zoomed view (marked with a red box). Data are expressed as mean ± S.D. (n = 3 measurements).

min^{-1} was applied to achieve rapid modulation of O_2 within the fluid channel.

With the determined total flow rate, the O_2 switching performance was experimentally validated by imaging the fluorescence lifetime of the O_2-sensitive dye (tris(2,2′-bipyridyl)dichlororuthenium(II)hexahydrate, RTDP) inside the fluid channel with FLIM. Fig. 2D depicts O_2 concentration measured in the fluid channel after the gas exchange from 21% to 0% and *vice versa*. The supply gas diffused into the fluid rapidly, achieving 99% of the aimed conditions (corresponding to a residual O_2 concentration of 0.21% when switching from 21% to 0%) within 15 seconds in both switching directions. The O_2 level in the gas supply was also switched between 21% and 0% at various oscillation half-periods T' (T' = 60, 30, 10, 5, 2, 1, 0.5 min), showing the robust experimental O_2-level data when toggling between 21% and 0% at various T', as shown in Fig. S1.† These device characterization results ensure a fast gas exchange in the order of seconds in the developed microfluidic device.

E. coli growth in constant and homogeneous O_2 environments

The fabricated double-layer cultivation device was first employed to cultivate *E. coli* MG1655 under a range of constant O_2 levels, between 0% and 21%, to determine whether the impact of various O_2 levels on microbial growth can be spatiotemporally resolved at the single-cell level. *E. coli* is a facultative anaerobic bacterium that can grow under aerobic, microaerobic, and anaerobic conditions. As known, the O_2-limited growth is slower compared to the growth under O_2-rich environments.[22]

Fig. 3A and B show representative time series of phase contrast images of *E. coli* cultivated under aerobic (21% O_2) and anaerobic (0% O_2) conditions. Both cultivations started with a single cell at 00:00 h, with a resulting larger colony area at 21% O_2 after 03:00 h cultivation time.

To further investigate whether various O_2 concentrations also result in a corresponding decrease in cell growth in the microfluidic growth chambers, we cultured *E. coli* under constant O_2 concentrations at 0%, 0.1%, 0.5%, 1%, 5%, 10%, and 21% O_2 in separate experiments. As shown in Fig. 3C, the colony areas (A_{colony}), the sum of the individual cell areas, are quantified from the phase contrast time-lapse images. As evident from the plot, A_{colony} exhibits exponential growth, with the lowest rate being observed at 0% O_2.

In Fig. 3D, the exponential growth rates μ were quantified based on A_{colony} in the exponential growth phase, showing comparable growth at O_2 concentrations between 21% and 1%. The aerobic growth rate of around 2 fits the growth rate suggested in previous literature.[35] Conversely, μ strongly decreases when the O_2 level is below 0.5%. The relation of

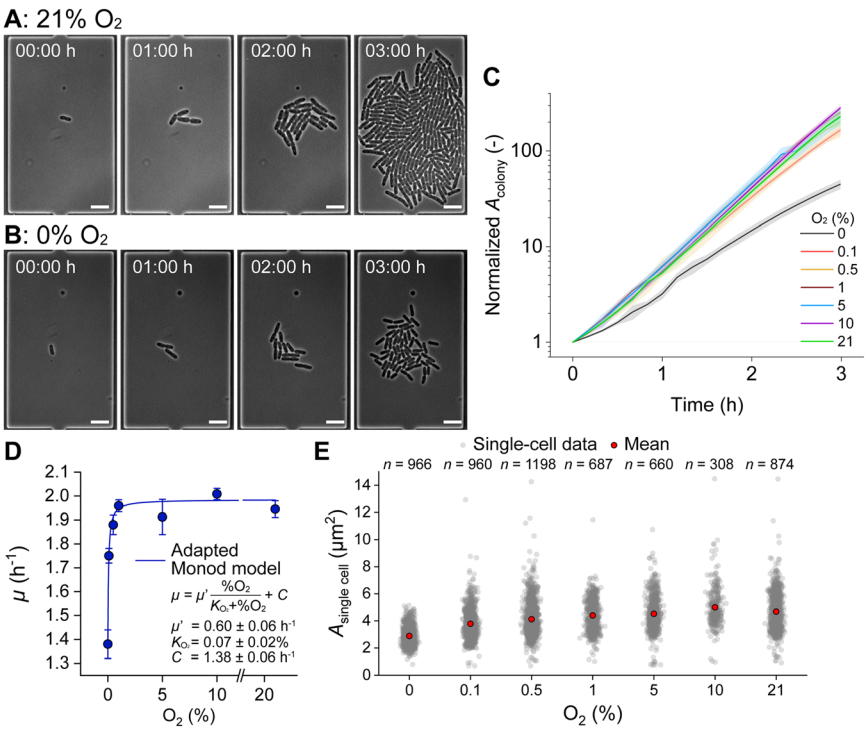

Fig. 3 *E. coli* cultivation under steady O_2 conditions. (A) Phase-contrast images of *E. coli* cultivated with a 21% O_2 supply (scale bars 5 μm). (B) Phase-contrast images of *E. coli* cultivated with a 0% O_2 supply (scale bars 5 μm). (C) Growth curves based on colony area (A_{colony}) under various O_2 levels. (D) Exponential growth rate (μ) under different O_2 levels, with the adapted Monod kinetic model fit shown by the blue line. (E) Single-cell area ($A_{single\ cell}$) across various O_2 levels at t = 2 h. Gray dots represent individual cell data, and red dots indicate mean values. The total numbers of analyzed cells are shown in the plot. In (C) and (D), data are expressed as mean ± S.D. n = 35 colonies (0%), 27 (0.1%), 21 (0.5%), 16 (1%), 13 (5%), 13 (10%), 29 (21%).

growth rate and O_2 concentration was modeled by an adapted Monod kinetic, which resulted in K_{O_2} of 0.07 ± 0.02%. As K_{O_2} describes the O_2 concentration in percentage at which the growth rate is reduced to half of the maximum growth under sufficient O_2, the low K_{O_2} indicates a strong decrease in growth rate at very low O_2 levels. These results indicate that an O_2 concentration of at least below 0.5% is required to observe a measurable change in the growth rate of *E. coli* within our device. Based on the gas exchange characterization shown in Fig. 2D, the minimum switching time, t_{min}, necessary to decrease O_2 concentration below 0.5% and observe a detectable change between aerobic and anaerobic growth was approximately 15 seconds. The slower growth observed at low O_2 concentration is in agreement with the Pasteur point (1% of the present atmospheric O_2 level), below which is thought to inhibit heterotrophic aerobic respiration.[36]

Beyond colony growth, our data also provide insights at the single-cell level. In Fig. 3E, each gray plot represents the area of an individual cell ($A_{single\ cell}$) measured at t = 2 h, with red plots representing the mean values. These mean values increase as oxygen concentration rises, which is consistent with the observation that cells with higher growth rates generally exhibit larger sizes.[37–39] Interestingly, $A_{single\ cell}$ displayed considerable variation, ranging up to 14 μm^2. This wide distribution suggests cell size heterogeneity within the population. Such heterogeneity in cell size might arise from a mixture of cells at different stages: smaller cells immediately post-division, larger cells just before division, and extensively sized cells with fewer division cycles. Such intra-population diversity can be effectively resolved using microfluidic cultivation combined with single-cell, time-lapse imaging.

E. coli growth in periodically oscillating O_2 environments

We then cultivated *E. coli* in oscillating O_2 environments to investigate how these oscillations affect bacterial growth.

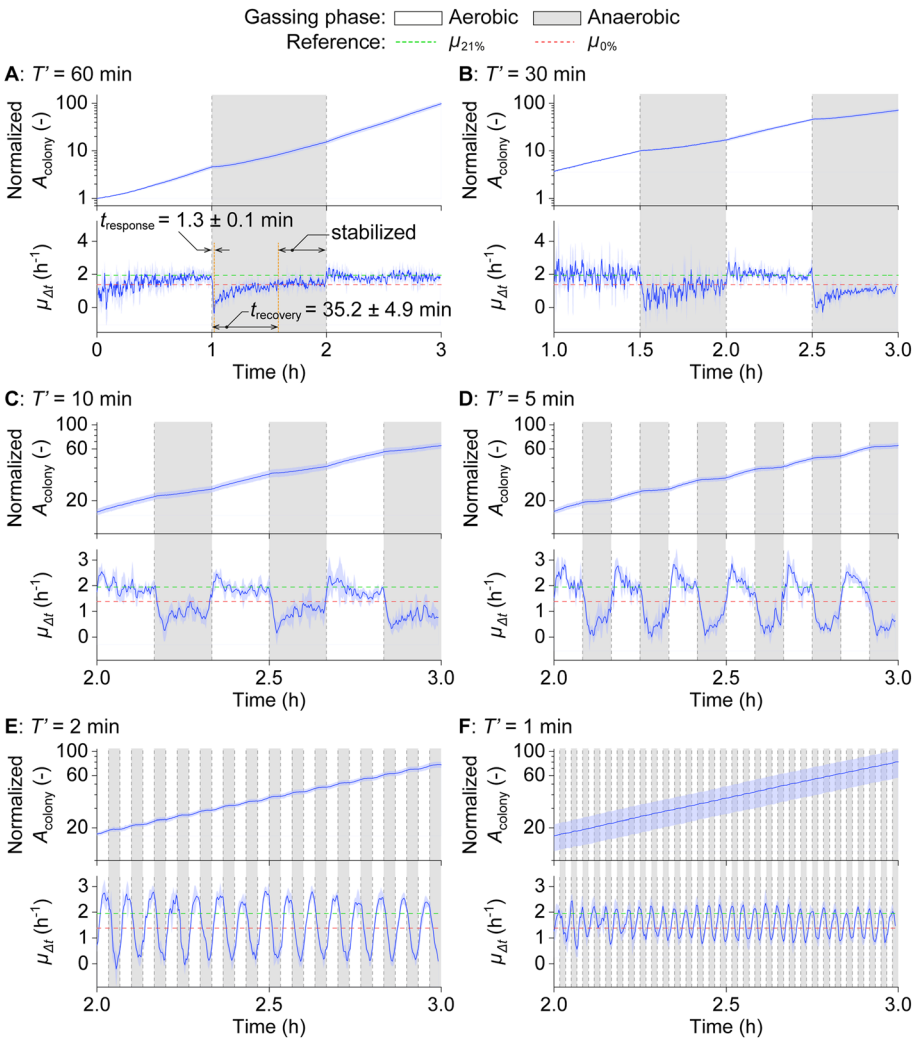

Fig. 4 *E. coli* cultivation under oscillating O_2 supplies. (A–F) Growth curves based on colony area (A_{colony}, top) and instantaneous growth rate ($\mu_{\Delta t}$, bottom) over time under various oscillation half-periods (T' = 60, 30, 10, 5, 2, and 1 min). Dashed lines represent growth rates under constant 21% ($\mu_{21\%}$) and 0% O_2 ($\mu_{0\%}$) conditions for comparison. Data are expressed as mean ± S.D. n = 5 colonies (60 min), 3 (30 min), 4 (10 min), 4 (5 min), 4 (2 min), 5 (1 min).

Experiments were conducted with various oscillation half-periods (T' = 60, 30, 10, 5, 2, and 1 min), and the results are presented in Fig. 4A–F (top: A_{colony}, bottom: instantaneous growth rate $\mu_{\Delta t}$). In Fig. 4A (top), the distinct growth rates during aerobic and anaerobic phases for each T' = 60 min cycle are observable from A_{colony}. The rate of change in A_{colony} was further quantified by $\mu_{\Delta t}$, calculated as the first derivative of ln A_{colony}. In Fig. 4A (bottom), a distinctive growth pattern under oscillating conditions emerges, where $\mu_{\Delta t}$ decreases directly after switching from aerobic to anaerobic conditions. A 1.2 fold decrease compared to growth at constant 0% O_2 conditions ($\mu_{0\%}$ = 1.38 ± 0.06 h^{-1}) occurs, followed by a gradual increase up to around $\mu_{0\%}$. We determined $t_{response}$, the time to hit the lowest $\mu_{\Delta t}$, and $t_{recovery}$, the time required to recover up to $\mu_{0\%}$, both counting from the switch from aerobic to anaerobic gassing phase. $t_{response}$ and $t_{recovery}$ are determined to be 1.3 ± 0.1 minutes and 35.2 ± 4.9 minutes, respectively. After $t_{recovery}$, the growth was stabilized around $\mu_{0\%}$ till the end of the anaerobic gassing phase. After the switch from anaerobic to aerobic gassing phase, in contrast, A_{colony} increased rapidly, reaching the growth rate at constant 21% O_2 concentration ($\mu_{21\%}$ = 1.95 ± 0.03 h^{-1}) within a minute.

At T' = 30 min, $\mu_{\Delta t}$ shows a growth tendency similar to T' = 60 min, characterized by the steep decrease right after the switch from aerobic to anaerobic conditions, and the following growth recovery till the end of the anaerobic gassing phase, as shown in Fig. 4B. At T' = 10, 5, and 2 min, we observe $\mu_{\Delta t}$ hitting the lowest value, and the following gradual recovery phase, but never reaching $\mu_{0\%}$, simply due to insufficient time for recovery and adaptation, as shown in Fig. 4C–E. In the case of T' = 2 min, only a brief recovery phase is observed after the response phase. At T' = 1 min, the steep decrease after the switch from aerobic to anaerobic conditions is observed without a recovery phase, followed by a fast increase right after the switch from anaerobic to aerobic conditions, as shown in Fig. 4F. As a result, the $\mu_{\Delta t}$ line plots at T' = 2 min and 1 min represent simpler waveforms (monotonous up and down) compared to the other cases.

The single-cell area also exhibited a distinct increase under aerobic and anaerobic gassing phases. Fig. S2A–F† are plotted with $A_{single\ cell}$ obtained from individual cells growing in a representative chamber of each oscillation condition. Fig. S2† allows us to speculate how individual cells increase their cell size by following neighboring plots without needing cell tracking that requires more complicated analytical setups. As for overall tendencies, the plots show a faster area increase rate under aerobic than anaerobic gassing phases, similar to colony-area analysis. A rapid increase/decrease in $A_{single\ cell}$ was observed immediately after each gassing switch across all oscillation conditions. Notably, a clear recovery in $A_{single\ cell}$ was observed when the oscillation half-periods were sufficiently longer than $t_{response}$ (T' = 60, 30, and 10 min).

Periodic growth synchronized with applied O_2 oscillations

To compare and examine further the periodic growth behavior induced by different O_2 oscillations, growth data is averaged over periods and plotted over the period fraction, as shown in Fig. 5A. Growth data with more than three periods (T' = 10, 5, 2, and 1 min) were analyzed.

The periodical comparison suggests that $\mu_{\Delta t}$ line plots from T' = 2 and 1 min have simpler waveforms compared to the other T' that are sufficiently longer than $t_{response}$. To examine the waveform complexity of $\mu_{\Delta t}$ line plots at various T', the frequency spectrum of $\mu_{\Delta t}$ line plots were analyzed using the fast Fourier transform (FFT) as shown in Fig. 5B. There are several frequency peaks at T' = 10 and 5 min. These several peaks imply the complicated waveform of $\mu_{\Delta t}$ line plots due to the existence of response and recovery phases. In contrast, there is only one frequency peak at T' = 2 and 1 min. The single peaks imply the simpler $\mu_{\Delta t}$ line plots, representing only the response phase. Notably, the highest peaks from FFT corresponded to applied O_2 oscillation half-periods T', showing that the periodic growth dynamics were synchronized with applied O_2 oscillation periods (T' = 10

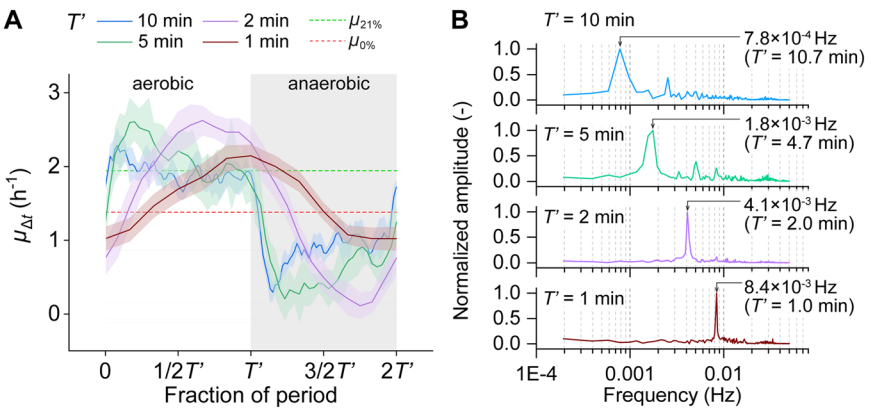

Fig. 5 Periodic growth dynamics synchronized with applied O_2 oscillations at various T'. (A) $\mu_{\Delta t}$ plotted over fractions of the oscillation period ($2T'$). Data are expressed as mean ± S.D. across periods. n = 6 (10 min), 12 (5 min), 30 (2 min), 60 (1 min). (B) Frequency spectrum of $\mu_{\Delta t}$ at T' = 10, 5, 2, and 1 min, obtained through fast Fourier transform (FFT).

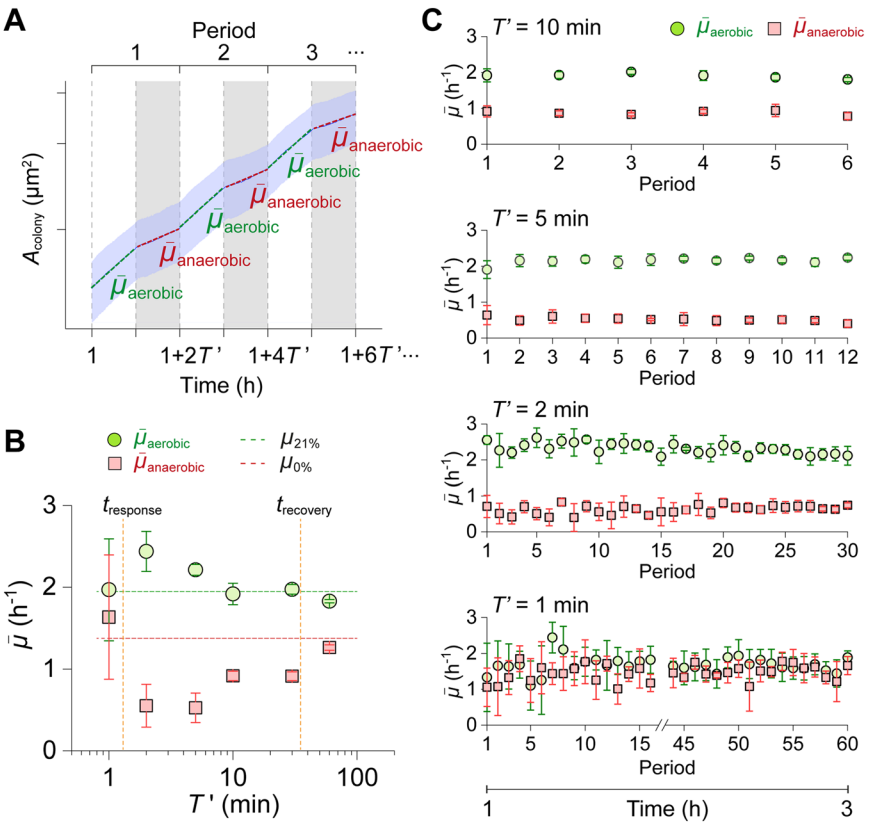

Fig. 6 Comparison of phase growth data across different T'. (A) Phase-averaged growth rates for each T', calculated for aerobic gassing phases ($\bar{\mu}_{aerobic}$) and anaerobic gassing phases ($\bar{\mu}_{anaerobic}$). (B) $\bar{\mu}_{aerobic}$ and $\bar{\mu}_{anaerobic}$ across different T', with data taken from periods starting at t = 2 h. For T' = 60 min, growth rate values are taken from half-periods beginning at t = 1 h (anaerobic) and 2 h (aerobic). Dashed lines represent growth rates under constant 21% ($\mu_{21\%}$) and 0% O_2 ($\mu_{0\%}$) conditions for comparison. (C) Time course of $\bar{\mu}_{aerobic}$ and $\bar{\mu}_{anaerobic}$ over multiple periods, illustrating robust growth behavior under oscillatory conditions. (B and C) Data are expressed as mean ± S.D. n = 5 colonies (60 min), 3 (30 min), 4 (10 min), 4 (5 min), 4 (2 min), 5 (1 min).

min: 7.8×10^{-4} Hz, T' = 5 min: 1.8×10^{-3} Hz, T' = 2 min: 4.1×10^{-3} Hz, T' = 1 min: 8.4×10^{-3} Hz).

Distinct growth behavior dependent on aerobic/anaerobic gassing phases

To further analyze the O_2-oscillation-dependent growth behavior, we determined phase-averaged growth rates under aerobic and anaerobic gassing phases ($\bar{\mu}_{aerobic}$, $\bar{\mu}_{anaerobic}$) by calculating the growth rate for each T', as illustrated in Fig. 6A.

In Fig. 6B, $\bar{\mu}_{aerobic}$ and $\bar{\mu}_{anaerobic}$ for each T' are summarized. At T' = 60 min, $\bar{\mu}_{aerobic}$ and $\bar{\mu}_{anaerobic}$ are comparable to $\mu_{21\%}$ and $\mu_{0\%}$ respectively, indicating the sufficient recovery time and growth stabilization after the gassing phase shift. At T' = 30 and 10 min, $\bar{\mu}_{aerobic}$ is comparable to $\mu_{21\%}$, whereas $\bar{\mu}_{anaerobic}$ is below $\mu_{0\%}$. This is due to insufficient recovery time under the anaerobic phases ($t_{response} < T' < t_{recovery}$), resulting in an overall lower growth rate over anaerobic phases. This trend became more obvious at T' = 5 and 2 min, with lower $\bar{\mu}_{anaerobic}$ because of less time for growth recovery. Interestingly, $\bar{\mu}_{aerobic}$ was higher than $\mu_{21\%}$ at T' = 5 and 2 min. This high $\bar{\mu}_{aerobic}$ is the result of the steep increase in growth rate right after the switch from anaerobic to aerobic gassing phases and insufficient time to adjust the growth rate to around $\mu_{21\%}$, as shown in Fig. 4D and E. Lastly, $\bar{\mu}_{aerobic}$ and $\bar{\mu}_{anaerobic}$ at T' = 1 min were close to each other, implying the growth adaptation attempt back and forth between aerobic and anaerobic phases, although insufficient time to adapt to either of gassing phases ($T' < t_{response}$). These results demonstrate a phase- and oscillation-period-dependent growth behavior that can be classified into several cases by growth characteristic values, $t_{response}$ and $t_{recovery}$.

Furthermore, we investigated the difference in phase-averaged growth rate over periods to examine the growth robustness under repeated O_2 oscillations. Growth data with more than 3 periods were analyzed (T' = 10, 5, 2, and 1 min). As shown in Fig. 6C, $\bar{\mu}_{aerobic}$ and $\bar{\mu}_{anaerobic}$ plotted over periods exhibit robust and steady trends, even with repetitive 60 periods at T' = 1 min. This result indicates the versatility of the developed platform to stably create O_2 oscillating conditions and analyze microbial growth under such conditions.

Discussion

The objective of this study was to investigate the growth dynamics of *E. coli* under oscillating O_2 environments. Previous

research on microbial growth response to gaseous changes has been extensively conducted, but predominantly focused on single shifts in O_2 availability. This restriction has resulted in our limited understanding of microbial growth response to O_2 fluctuations. To facilitate further investigation, we developed the double-layer microfluidic platform for the time-lapse monitoring of microbes under rapidly oscillating O_2 environments. The platform enabled the cultivation of microbes under well-defined on-chip O_2 oscillating environments and simultaneous observation of microbial behavior at high spatiotemporal resolution. Our platform enabled the thorough analysis of the growth dynamics of *E. coli* based on growth rates in different time scales (μ, $\bar{\mu}$, $\mu_{\Delta t}$). While single-cell analysis is known for its high workload required to extract biological information such as growth rates at the single-cell level, it turned out to be crucial to establish fully automated image analysis and data extraction prior to the development of the microfluidic device. Based on these analysis procedures, we quickly iterated and adapted our microfluidic chip prototypes and directly verified the effects based on the biological outputs with only overnight delay. This high walkaway time and high throughput experimentation allowed us to primarily focus on optimizing the microfluidic chip design and experiment preparation while biological insights were automatically extracted. Such a single-cell analysis of continuous microbial growth under oscillating O_2 environments with high temporal resolution was impossible with conventional analytical platforms.

The thorough growth analysis presented here demonstrates distinct growth dynamics induced by O_2 oscillations, which are characterized by an immediate decrease in $\mu_{\Delta t}$ after the switch from aerobic to anaerobic gassing phases (response), followed by gradual increase (recovery), and later stabilized state. These distinguished cell behaviors occur depending on oscillation half-periods T'. This is reasonable, considering that the change from one metabolic pathway to another requires a series of biological events, such as signal transduction (in milliseconds), enzymatic reaction (in seconds), transcription (in minutes), and translation (in minutes), occurring at different time scales.[26,40,41] For example, the O_2 oscillation with $T' = 1$ min was sufficient to rapidly and strongly decrease the *E. coli* growth rates in the respective anaerobic gassing phase (Fig. 4F). This observation could be explained by the rapid depletion of the ATP pool under O_2 limitation, which occurs within the time scale of microbial responses to environmental fluctuations associated with enzymatic reactions and metabolite turnover under minute.[26] A recurring increase in the *E. coli* growth rates were observed when $T' > t_{\text{response}}$ (Fig. 4A–D). This adaptation to prolonged anaerobic phases is most likely the result of specific regulatory processes that alter gene expression patterns, leading to a gradual change in cell metabolism in minutes.[25] Under the switch from anaerobic to aerobic gassing phases, the initial peak and the subsequent gradual decrease of $\mu_{\Delta t}$ was also observed. This temporal change in growth rate may be attributed to transient accumulation or excretion of metabolites as a result of maintaining homeostasis upon the gaseous transition in minutes.[23,42] Lastly, the FFT and phase-averaged growth rate analyses revealed periodic and robust growth dynamics synchronized with the applied O_2 oscillation periods. This result implies the cellular capability to respond and adapt to corresponding extracellular O_2 environments and highlights the importance of O_2 in determining cellular growth behavior. Regarding the metabolic switching under aerobic and anaerobic conditions, hybrid metabolism has been reported under microaerobic conditions, where both aerobic and anaerobic metabolisms are utilized.[25,43] Therefore, metabolic switching is a continuous process that may not be clearly divided into aerobic and anaerobic states. Rather, the switching time of *E. coli* can be characterized and determined by various biological events, as mentioned earlier. For instance, the timescales of enzymatic reaction, transcription, and translation would fit our study. Follow-up studies would be valuable to further investigate the correlation between the biological timescales and O_2 fluctuation timescales.

The demonstrated experiment and analysis platform can be strengthened with further improvements. In our platform, we measured the fluorescence lifetimes at 0% and 0.1% O_2, which can be distinguished from each other. However, we have not yet made any further measurements in the range below 0.1%. Obviously, O_2 sensing with the O_2 indicator and FLIM has its limits in terms of sensitivity, which is a complex technical issue that depends on several parameters. For example, the measurement may be affected by the accuracy and resolution of the O_2 control. A set of mass flow controllers connected to pure N_2 and O_2 gas supply was used in our setup, which also has limitations in resolution, especially at lower O_2 concentrations below 0.1%, where the mass flow rate has to be set very low compared to an ideal operating range. A follow-up study should consider using a gas supply with a lower O_2 concentration (for instance, 1%) instead of pure O_2 gas so that the mass flow controller can operate in the recommended flow range when controlling O_2 concentrations below 0.1%. FLIM and the O_2 sensing dye can be characterized with such an improved setup for O_2 control. Finally, sensitivity can be determined with finer resolution at low O_2 concentrations. Another factor is the two-point calibration at known O_2 availability. This calibration was done by flushing synthetic air containing either 0% or 21% O_2. While controlling the O_2 availability to 21% was credible, achieving a strict O_2 control at 0% remained challenging due to potential disturbances from high air permeability and the possibility of residual air remaining within the PDMS. By improving the calibration method to ensure strict 0% O_2 availability, such as by using chemical O_2 scavengers[44–46] compatible with the O_2-sensitive chemical or by using a mini-incubator that allows flushing O_2 depleted gas around the PDMS chip,[47] more precise on-chip O_2 control and sensing under anaerobic conditions may be possible to achieve.

The developed device and the finding regarding microbial behavior under O_2 oscillation have the potential to be applied to a wide range of research fields. In terms of practical applications, the findings are useful in characterizing and

improving industrial bioprocesses. The fluctuating environments resulting from heterogeneous conditions in large-scale bioreactors have been widely reported, which result in unexpected inefficiency and yield losses.[13–15] Such fluctuations in industrial bioreactors, specifically O_2 fluctuations, can occur under minutes.[48] To address this issue, it is of the utmost importance to gain a further understanding of microbial behavior under rapid fluctuating environments. The developed device provides an on-chip environment that mimics rapid O_2 fluctuations inside bioreactors. This enables the analysis of O_2 fluctuation-specific microbial behavior, including the emerging phenotypic heterogeneity at single-cell resolution, which was previously not possible.

A comparable approach to recreate fluctuating O_2 environments and live-cell imaging could also prove beneficial in fundamental biology and biomedicine. For instance, it is of interest to investigate pathogenic microorganisms (for example, *Salmonella typhimurium*) and their mechanism on virulence expression and host-cell infection. It has been recognized that pathogens use O_2 as a signal to trigger their virulence, yet the underlying mechanism is elusive.[18,49] Our analysis platform provides an optimal environment for such a study, where microbial behavior can be resolved at single-cell resolution under a well-defined O_2 environment. Another example is to study the interaction of gastrointestinal host cells and microbial communities under fluctuating O_2 environments. There has been growing evidence that O_2 dynamics play a pivotal role in maintaining intestinal homeostasis.[50,51] The intricate regulatory mechanisms at the interface of host cells and the microbiome and the role of O_2 are of great interest since these interactions are linked to various diseases.[51] Moreover, several reports imply the existence of O_2 fluctuations in the intestine and the intestinal epithelial–microbiome interface that arise from periodic ingestion of nutrients or intermittent changes in O_2 availability in the blood.[52–54] Based on these previous reports, it is reasonable to assume that the timescale of O_2 fluctuations for gut microbiome would be in the range of hours. In fact, previous research reported fluctuating bacterial abundance in wild meerkats throughout the day, with the relative abundance of aerobic (*Cellulomonas*) and anaerobic microbes (*Clostridium*) varying due to changes in O_2 availability during that time.[55] The presented device and analysis could be applied to study the interplay between host epithelial cells and microbiomes by emulating such an O_2 fluctuating environment.

Materials and methods

Microfluidic device fabrication

The double-layer microfluidic device, comprising an upper and a lower layer, was fabricated by molding PDMS in separate molds and by assembling (Fig. 2A).[56] Firstly, the mold for the upper layer was prepared by 3D printing with stereolithography (Form 3B, Formlabs, US). The mold was filled with a mixture of pre-cured PDMS solution (10 : 1) and heated to 80 °C for 20 minutes to initiate the first curing step. A silicon wafer with a two-layer SU-8 photoresist was fabricated by photolithography as described in a previous paper[57] at Helmholtz Nano Facility, Germany[58] and employed as the mold for the lower layer. The PDMS was spin-coated onto the SU-8 mold at 1000 rpm for 60 seconds (SPIN150i, APT Automation, Germany) and subsequently heated at 80 °C for 10 minutes to initiate the first curing step. Then, the upper layer was peeled off from the mold, cut into chips, and inlets were punched (punching tool φ = 0.75 mm, World Precision Instruments, US). The lower layer was not peeled off at this step. The upper layer was then placed onto the lower layer and heated at 80 °C for a minimum of one hour. This constituted the second curing step, whereby the upper and lower layers were irreversibly bonded together through the full curing process. Once fully cured, the chip was peeled off from the wafer, holes were punched (φ = 0.50 mm, World Precision Instruments, US), and bonded to a glass substrate (D263®Bio, 39.5 mm × 34.5 mm × 0.175 mm; Schott AG, Germany) by O_2 plasma treatment for 25 seconds (Femto Plasma Cleaner, Diener Electronics, Germany). The bonded chip was heated at 80 °C for one minute to increase the stability of the bonding.

Computational simulations

The gas distribution in the PDMS chip was simulated using a finite element method (COMSOL Multiphysics 6.0, COMSOL). A three-dimensional geometrical model was built comprising three distinct subdomains, a PDMS block, a fluid channel, and a gas channel (Fig. S3†). A hexahedral mesh was generated for the fluid channel, while a tetrahedral mesh was generated for the remaining geometry. The physical phenomena of fluid flow and gas flow were numerically analyzed by solving the time-dependent Navier–Stokes equations for laminar and incompressible flow. O_2 transport was determined by diffusion and convection, as well as by the ratios between O_2 concentration and O_2 solubility at the different material boundaries. Further details regarding the simulation setup are described in the ESI.†

Microscopy

An inverted microscope (Nikon Eclipse Ti-E 2, Nikon, Japan), equipped with a CMOS camera (DS-Qi2, Nikon, Japan) for phase-contrast image acquisition and a FLIM camera (550 kHz frequency domain; pco.flim, PCO AG, Germany), was utilized for the experiments. The FLIM camera was connected to a modulated excitation laser (445 nm, 100 mW; pco.flim laser, Omicron-Laserage Laserprodukte GmbH, Germany). The microscopy setup was customized with a perfect focus system (PFS, Nikon, Japan) and a temperature incubator (Okolab, Italy) to facilitate automated live-cell imaging during cell cultivation on the microscope. Phase-contrast observation for biological cultivation was conducted with a 100× objective (Plan Apo λ Oil, Nikon, Japan). FLIM imaging was conducted with a 20× objective (Plan Apo λ, Nikon, Japan). To perform FLIM, a customized filter cube was used, which was

composed of an excitation filter (440/40, F47-440), a long-pass dichroic mirror (495LP, F48-495), and an emission filter (605/70, F47-605). All the filter components were purchased from AHF analysentechnik AG, Germany. A custom-made chip holder was used to mount the chip on the microscope stage. The FLIM was calibrated using a reference fluorescent slide with a known lifetime (lifetime = 3.75 ns, UMM-SFG, Starna Scientific, UK) as a standard. Further details are described in a previously published paper.[47]

Gas control and O_2 sensing

Three interconnected mass flow controllers were utilized to continuously deliver the synthetic air mixture with the desired concentrations of N_2, O_2, and CO_2 (red-y, Vögtlin Instruments GmbH, Switzerland). For on-chip gas control, the inlet of the gas channel was connected to the mass flow controllers. The desired O_2 concentrations in the gas supply were achieved by automatically adjusting the corresponding volume flow rates for O_2 and N_2 while maintaining the total flow rate constant at 600 mL min^{-1} throughout the oscillations. 0.4 mL min^{-1} of CO_2 was always added to the synthetic air to facilitate reproducible growth of *E. coli*.[59] A tubing with a low gas permeability (N_2: 1.2 barrer, O_2: 2.2 barrer; Tygon®F-4040-A, Saint-Gobain, France) was used to connect the mass flow controller and the hole on the upper layer of the chip. To measure O_2 concentrations of in-flow coming out of the tubing, a fiber O_2 microsensor was used and inserted directly in the tubing (OXR50, pyroscience, Germany).

The O_2 level in the chip was measured by fluorescence lifetime imaging (FLIM) and an O_2-sensitive dye, tris(2,2′-bipyridyl)dichlororuthenium(II)hexahydrate (RTDP). The fluorescence of RTDP is quenched in the presence of O_2, which can be quantified as a change in fluorescence lifetime (τ). The fluorescence quenching is described by the Stern–Volmer equation, as follows.

$$[O_2] = \frac{1}{K_q}\left(\frac{\tau_0}{\tau} - 1\right) \quad (1)$$

τ_0 is the fluorescence lifetime under 0% O_2, and K_q is the quenching constant. K_q was derived by a two-point calibration, whereby τ_0 and τ at a known O_2 concentration were measured. Here, τ at 21% O_2 (τ_{21}) was used to derive K_q. The gaseous conditions of 0% and 21% O_2 were set by adjusting the mass flow rate of N_2 and O_2. The parameters were determined from the measurement as follows; τ_0 = 481 ns, τ_{21} = 307 ns, K_q = 2.71.

Cell preparation

E. coli MG1655 was stored in a ROTI Store cryo vial (ROTI®Store cryo vial, Carl Roth, Germany). All microbial cultivations were conducted using a lysogeny broth (LB) complex medium, comprising 10 g L^{-1} peptone, 5 g L^{-1} yeast extract, and 10 g L^{-1} NaCl. The pH of the LB medium was adjusted to 7.0 with NaOH, autoclaved at 121 °C for 20 minutes, and stored at 4 °C. All the aforementioned chemicals were purchased from Carl Roth, Germany. A single bead from the cryo vial was transferred to a 20 mL LB medium in a shaking flask and cultured at 37 °C, 150 rpm, for around 16 hours. The subsequent culture was initiated by inoculation from the previous culture, with an initial optical density (OD_{600}) of 0.3 or 0.0001, and cultivated until it reached the exponential growth phase.

Microfluidic cultivation and time-lapse imaging

The inoculation in the microfluidic chip was performed with the cell solution containing exponentially growing cells, with OD_{600} = 0.5. The cell solution was introduced into the fluid channel of the chip with a syringe (Omnifix®-F 1 mL, Braun, Germany). Following the successful inoculation, the syringe was replaced with a new one containing a fresh medium. The remaining cells within the channel were then flushed by manually pushing the syringe. The medium was perfused at a constant rate of 100 nL min^{-1} using a syringe pump (neMESYS, CETONI, Germany). The chip cultivation continued for three hours before the colony reached the chamber size. The time-lapse imaging was performed, with an image acquisition interval Δt = 1 min for all the cultivation under constant O_2 environments, and Δt = 10 seconds for all the cultivation under oscillating O_2 environments.

Image analysis

The acquired FLIM image data in nd2 format was saved as OME.TIFF files and processed using Fiji[60] to measure the lifetime in a rectangular ROI (h 500 pixels × w 100 pixels). A median filter (pixel size = 5) was employed to remove noise.

The details of the image analysis from cultivation experiments are described in previously published papers.[47,61] Briefly, the acquired image data in nd2 format was exported as TIFF files and pre-processed using Fiji, which included rotation, alignment (Correct 3D Drift[62]), and cropping. The pre-processed TIFF files were then uploaded to an OMERO server[63] for subsequent analysis. For the automated image analysis, we developed Jupyter Notebooks and Python to perform deep-learning-based cell segmentation (Omnipose[64]) followed by filtering artifacts and extracting single-cell sizes. These Jupyter Notebooks are designed for a single time-lapse recording and provide video rendering to guarantee and document sufficient cell segmentation quality. We repeatedly apply the same Jupyter Notebook to all our timelapse images (scaling analysis), leading to fully automated image processing such that experiment results are obtained overnight. The codes for cell segmentation and analysis are openly available at **https://github.com/JuBiotech/Supplement-to-Kasahara-et-al.-2025**.

Growth analysis

Colony area (A_{colony}) was used for growth analysis because A_{colony} provides us with continuous values as opposed to cell number, which is beneficial for further calculations. A_{colony}

was normalized by the colony area at the start of cultivation to compare different chambers and conditions. Exponential growth rates, μ, were quantified based on A_{colony} in the exponential growth phase, as follows.

$$\mu = \frac{\ln A_{\text{colony},\,t} - \ln A_{\text{colony},\,t_0}}{t - t_0} \quad (2)$$

The relation of growth rate and O_2 concentration was modeled by a Monod kinetic[65] including a growth offset for anaerobic growth, C (h^{-1}) at 0% O_2, as follows.

$$\mu = \mu' \frac{\%\ O_2}{K_{O_2} + \%\ O_2} + C \quad (3)$$

$\mu' + C$ (h^{-1}) is the growth rate under high O_2 availability, and K_{O_2} is the so-called Michaelis–Menten constant.

Instantaneous growth rates, $\mu_{\Delta t}$, the first derivative of A_{colony}, were calculated as follows.

$$\mu_{\Delta t} = \frac{\ln A_{\text{colony},\,t+\Delta t} - \ln A_{\text{colony},\,t-\Delta t}}{2\Delta t} \quad (4)$$

Phase-averaged growth rates under aerobic and anaerobic gassing phases ($\bar{\mu}_{\text{aerobic}}$ and $\bar{\mu}_{\text{anaerobic}}$), were determined by averaging obtained values from the same periods in all the analyzed colonies. t_{response} was determined as the time to hit the lowest $\mu_{\Delta t}$. t_{recovery} was determined as the time for the linear regression slope of $\mu_{\Delta t}$ in a shrinking window to reach zero.

The fast Fourier transform (FFT) was performed using the Data Analysis Tools in Excel. The sample size was adjusted to 2^n prior to FFT. For all the growth analysis, growth data between 0 h $\leq t <$ 1 h were omitted since growth data at the beginning of the cultivation was occasionally affected by high noise due to a low initial cell number. Datasets with Δt = 10 seconds were smoothed by a centered moving average (window size = 5) before calculating $\mu_{\Delta t}$ to reduce noise.

Data availability

The codes for image analysis are available at **https://github.com/JuBiotech/Supplement-to-Kasahara-et-al.-2025**. Microscopy image data are available at **https://doi.org/10.5281/zenodo.13982747**.

Author contributions

K. K. and D. K. designed the study. K. K. conducted the experiments and data analyses. K. K., T. D., and D. K. interpreted the results. J. S. and K. N. contributed to the automated image workflows and data management. B. S. and E. L. conducted the numerical simulation. K. K., T. D., and D. K. wrote the paper. All authors contributed to the article and approved the submitted version.

Conflicts of interest

The authors declare that the research was conducted in the absence of any commercial or financial relationships that could be construed as a potential conflict of interest.

Acknowledgements

K. K. was supported by the Japan Student Services Organization (JASSO) Student Exchange Support Program (G2130401003N). K. K. is an associate member of the SFB 1535 MibiNet "Microbial networking – from organelles to cross-kingdom communities" funded by the Deutsche Forschungsgemeinschaft (DFG, German Research Foundation, 458090666/CRC1535/1). J. S. was supported by the President's Initiative and Networking Funds of the Helmholtz Association of German Research Centres (EMSIG ZT-I-PF-04044). J. S. and K. N. acknowledge the inspiring scientific environment provided by the Helmholtz School for Data Science in Life, Earth and Energy (HDS-LEE). The authors would like to thank Agnes Müller-Schröer (Forschungszentrum Jülich) for her assistance in cell culture and Nadja Glöck (Forschungszentrum Jülich) for her assistance in SU-8 mold fabrication.

References

1 A. Lalejini, A. J. Ferguson, N. A. Grant and C. Ofria, *Front. Ecol. Evol.*, 2021, **9**, 715381.
2 M. Fusi, S. Rigaud, G. Guadagnin, A. Barausse, R. Marasco, D. Daffonchio, J. Régis, L. Huchet, C. Camin, L. Pettit, C. Vina-Herbon and F. Giomi, *Biogeosciences*, 2023, **20**, 3509–3521.
3 R. Stocker, *Science*, 2012, **338**, 628–633.
4 S. Dedrick, M. J. Akbari, S. K. Dyckman, N. Zhao, Y.-Y. Liu and B. Momeni, *Front. Microbiol.*, 2021, **12**, 613109.
5 Y. Zhang, J.-T. Li, X. Xu, H.-Y. Chen, T. Zhu, J.-J. Xu, X.-N. Xu, J.-Q. Li, C. Liang, B. Li, C.-M. Fang and M. Nie, *Nat. Ecol. Evol.*, 2023, **7**, 205–213.
6 E. Cohen Susan and S. Golden Susan, *Microbiol. Mol. Biol. Rev.*, 2015, **79**, 373–385.
7 F. Formenti, N. Bommakanti, R. Chen, J. N. Cronin, H. McPeak, D. Holopherne-Doran, G. Hedenstierna, C. E. W. Hahn, A. Larsson and A. D. Farmery, *Sci. Rep.*, 2017, **7**, 1–10.
8 C. A. Lozupone, J. I. Stombaugh, J. I. Gordon, J. K. Jansson and R. Knight, *Nature*, 2012, **489**, 220–230.
9 D. J. Lodge, W. H. McDowell and C. P. McSwiney, *Trends Ecol. Evol.*, 1994, **9**, 384–387.
10 S. Smriga, V. I. Fernandez, J. G. Mitchell and R. Stocker, *Proc. Natl. Acad. Sci. U. S. A.*, 2016, **113**, 1576–1581.
11 N. Blackburn, T. Fenchel and J. Mitchell, *Science*, 1998, **282**, 2254–2256.
12 J. R. Taylor and R. Stocker, *Science*, 2012, **338**, 675–679.
13 S. O. Enfors, M. Jahic, A. Rozkov, B. Xu, M. Hecker, B. Jürgen, E. Krüger, T. Schweder, G. Hamer, D. O'Beirne, N. Noisommit-Rizzi, M. Reuss, L. Boone, C. Hewitt, C. McFarlane, A. Nienow, T. Kovacs, C. Trägårdh, L. Fuchs, J.

Revstedt, P. C. Friberg, B. Hjertager, G. Blomsten, H. Skogman, S. Hjort, F. Hoeks, H. Y. Lin, P. Neubauer, R. van der Lans, K. Luyben, P. Vrabel and A. Manelius, *J. Biotechnol.*, 2001, **85**, 175–185.
14 R. Takors, *J. Biotechnol.*, 2012, **160**, 3–9.
15 J. Bisgaard, M. Muldbak, T. Tajsoleiman, T. Rydal, T. Rasmussen, J. K. Huusom and K. V. Gernaey, *Chem. Eng. Res. Des.*, 2021, **174**, 471–485.
16 M. Miethke and M. A. Marahiel, *Microbiol. Mol. Biol. Rev.*, 2007, **71**, 413–451.
17 E. Cabiscol, J. Tamarit and J. Ros, *Int. Microbiol.*, 2000, **3**, 3–8.
18 A. C. André, L. Debande and B. S. Marteyn, *Cell. Microbiol.*, 2021, **23**, e13338.
19 A. J. Martín-Rodríguez, *Trends Microbiol.*, 2023, **31**, 120–134.
20 J. D. Partridge, C. Scott, Y. Tang, R. K. Poole and J. Green, *J. Biol. Chem.*, 2006, **281**, 27806–27815.
21 T. Ren, X. Jin, S. Deng, K. Guo, Y. Gao, X. Shi, L. Xu, X. Bai, Y. Shang, P. Jin and X. C. Wang, *J. Cleaner Prod.*, 2024, **434**, 140332.
22 O. N. Murashko and S. Lin-Chao, *Proc. Natl. Acad. Sci. U. S. A.*, 2017, **114**, E8025–E8034.
23 N. A. Yasid, M. D. Rolfe, J. Green and M. P. Williamson, *R. Soc. Open Sci.*, 2016, **3**, 160187.
24 J. von Wulffen, RecogNice-Team, O. Sawodny and R. Feuer, *PLoS One*, 2016, **11**, e0158711.
25 L. Pedraz, N. Blanco-Cabra and E. Torrents, *FASEB J.*, 2020, **34**, 2912–2928.
26 J. Nguyen, J. Lara-Gutiérrez and R. Stocker, *FEMS Microbiol. Rev.*, 2021, **45**, 1–16.
27 J. Nguyen, V. Fernandez, S. Pontrelli, U. Sauer, M. Ackermann and R. Stocker, *Nat. Commun.*, 2021, **12**, 3662.
28 M. Skolimowski, M. W. Nielsen, J. Emnéus, S. Molin, R. Taboryski, C. Sternberg, M. Dufva and O. Geschke, *Lab Chip*, 2010, **10**, 2162–2169.
29 G. Mauleon, C. P. Fall and D. T. Eddington, *PLoS One*, 2012, **7**, e43309.
30 M. L. Rexius-Hall, G. Mauleon, A. B. Malik, J. Rehman and D. T. Eddington, *Lab Chip*, 2014, **14**, 4688–4695.
31 S. M. Grist, S. S. Nasseri, L. Laplatine, J. C. Schmok, D. Yao, J. Hua, L. Chrostowski and K. C. Cheung, *Sci. Rep.*, 2019, **9**, 17782.
32 R. Koens, Y. Tabata, J. C. Serrano, S. Aratake, D. Yoshino, R. D. Kamm and K. Funamoto, *APL Bioeng.*, 2020, **4**, 016106.
33 S. Täuber, C. Golze, P. Ho, E. von Lieres and A. Grünberger, *Lab Chip*, 2020, **20**, 4442–4455.
34 Q. Tang, D. Wang, J. Cui, Y. Zhang, J. Mei, J. Du, A. Xia, Q. Sun, D. Luo, B. Han, M. Gan and P. Liu, *Nano Today*, 2024, **54**, 102067.
35 A. R. Tuttle, N. D. Trahan and M. S. Son, *Curr. Protoc.*, 2021, **1**, e20.
36 C. Goldblatt, T. M. Lenton and A. J. Watson, *Nature*, 2006, **443**, 683–686.
37 M. Schaechter, O. Maaloe and N. O. Kjeldgaard, *J. Gen. Microbiol.*, 1958, **19**, 592–606.
38 S. Taheri-Araghi, S. Bradde, J. T. Sauls, N. S. Hill, P. A. Levin, J. Paulsson, M. Vergassola and S. Jun, *Curr. Biol.*, 2015, **25**, 385–391.
39 F. Bertaux, J. von Kügelgen, S. Marguerat and V. Shahrezaei, *PLoS Comput. Biol.*, 2020, **16**, e1008245.
40 J. D. Partridge, G. Sanguinetti, D. P. Dibden, R. E. Roberts, R. K. Poole and J. Green, *J. Biol. Chem.*, 2007, **282**, 11230–11237.
41 J. von Wulffen, A. Ulmer, G. Jäger, O. Sawodny and R. Feuer, *Genes*, 2017, **8**, 90.
42 N. A. Beauchene, E. L. Mettert, L. J. Moore, S. Keleş, E. R. Willey and P. J. Kiley, *Proc. Natl. Acad. Sci. U. S. A.*, 2017, **114**, 12261–12266.
43 M. D. Rolfe, A. Ocone, M. R. Stapleton, S. Hall, E. W. Trotter, R. K. Poole, G. Sanguinetti, J. Green and SysMO-SUMO Consortium, *Open Biol.*, 2012, **2**, 120091.
44 W. Sun, Y. Chen, Y. Wang, P. Luo, M. Zhang, H. Zhang and P. Hu, *Analyst*, 2018, **143**, 5431–5437.
45 W. Wang, L. Li, M. Ding, G. Luo and Q. Liang, *BioChip J.*, 2018, **12**, 93–101.
46 H. M. Wu, T. A. Lee, P. L. Ko, W. H. Liao, T. H. Hsieh and Y. C. Tung, *Analyst*, 2019, **144**, 3494–3504.
47 K. Kasahara, M. Leygeber, J. Seiffarth, K. Ruzaeva, T. Drepper, K. Nöh and D. Kohlheyer, *Front. Microbiol.*, 2023, **14**, 1198170.
48 E. K. Nauha, Z. Kálal, J. M. Ali and V. Alopaeus, *Chem. Eng. J.*, 2018, **334**, 2319–2334.
49 B. Marteyn, F. B. Scorza, P. J. Sansonetti and C. Tang, *Cell. Microbiol.*, 2011, **13**, 171–176.
50 M. A. Henson and P. Phalak, *BMC Syst. Biol.*, 2017, **11**, 145.
51 R. Singhal and Y. M. Shah, *J. Biol. Chem.*, 2020, **295**, 10493–10505.
52 J. B. J. Ward, S. J. Keely and S. J. Keely, *J. Physiol.*, 2014, **592**, 2473–2489.
53 L. Zheng, C. J. Kelly and S. P. Colgan, *Am. J. Physiol.*, 2015, **309**, C350–C360.
54 I. Moreno-Indias, M. Torres, J. M. Montserrat, L. Sanchez-Alcoholado, F. Cardona, F. J. Tinahones, D. Gozal, V. A. Poroyko, D. Navajas, M. I. Queipo-Ortuño and R. Farré, *Eur. Respir. J.*, 2015, **45**, 1055–1065.
55 A. Risely, K. Wilhelm, T. Clutton-Brock, M. B. Manser and S. Sommer, *Nat. Commun.*, 2021, **12**, 6017.
56 M. Polinkovsky, E. Gutierrez, A. Levchenko and A. Groisman, *Lab Chip*, 2009, **9**, 1073–1084.
57 A. Grünberger, N. Paczia, C. Probst, G. Schendzielorz, L. Eggeling, S. Noack, W. Wiechert and D. Kohlheyer, *Lab Chip*, 2012, **12**, 2060–2068.
58 W. Albrecht, J. Moers and B. Hermanns, *JLSRF*, 2017, **3**, A112.
59 C. Merlin, M. Masters, S. McAteer and A. Coulson, *J. Bacteriol.*, 2003, **185**, 6415–6424.
60 J. Schindelin, I. Arganda-Carreras, E. Frise, V. Kaynig, M. Longair, T. Pietzsch, S. Preibisch, C. Rueden, S. Saalfeld, B. Schmid, J. Y. Tinevez, D. J. White, V. Hartenstein, K. Eliceiri, P. Tomancak and A. Cardona, *Nat. Methods*, 2012, **9**, 676–682.

61 J. Seiffarth, T. Scherr, B. Wollenhaupt, O. Neumann, H. Scharr, D. Kohlheyer, R. Mikut and K. Nöh, *SoftwareX*, 2024, **26**, 101638.
62 A. Parslow, A. Cardona and R. J. Bryson-Richardson, *J. Visualized Exp.*, 2014, e51086.
63 C. Allan, J.-M. Burel, J. Moore, C. Blackburn, M. Linkert, S. Loynton, D. MacDonald, W. J. Moore, C. Neves, A. Patterson, M. Porter, A. Tarkowska, B. Loranger, J. Avondo, I. Lagerstedt, L. Lianas, S. Leo, K. Hands, R. T. Hay, A. Patwardhan, C. Best, G. J. Kleywegt, G. Zanetti and J. R. Swedlow, *Nat. Methods*, 2012, **9**, 245–253.
64 K. J. Cutler, C. Stringer, T. W. Lo, L. Rappez, N. Stroustrup, S. Brook Peterson, P. A. Wiggins and J. Mougous, *Nat. Methods*, 2022, **19**, 1438–1448.
65 O. Couvert, M.-L. Divanac'h, A. Lochardet, D. Thuault and V. Huchet, *Food Microbiol.*, 2019, **77**, 21–25.